G331.512–0.103: An Interstellar Laboratory for Molecular Synthesis. I. The Ortho-to-para Ratios for CH₃OH and CH₃CN

Edgar Mendoza[1] , Leonardo Bronfman[2] , Nicolas U. Duronea[3], Jacques R. D. Lépine[1] , Ricardo Finger[2], Manuel Merello[4] ,
Carlos Hervías-Caimapo[2,5], Diana R. G. Gama[1] , Nicolas Reyes[6], and Lars Åke-Nyman[7]

[1] Universidade de São Paulo, IAG Rua do Matão, 1226, Cidade Universitária, 05508-090, São Paulo, Brazil; emendoza@usp.br
[2] Departamento de Astronomía, Universidad de Chile, Casilla 36-D, Santiago de Chile, Chile
[3] Instituto Argentino de Radioastronomía, IAR CONICET, CCT-La Plata, C.C.5., 1894, Villa Elisa, Argentina
[4] Istituto di Astrofisica e Planetologia Spaziali-INAF Via Fosso del Cavaliere 100, I-00133 Roma, Italy
[5] Jodrell Bank Centre for Astrophysics, School of Physics and Astronomy, University of Manchester, Oxford Road, Manchester M139PL, UK
[6] Electrical Engineering Department, Universidad de Chile, Av. Tupper 2007, Santiago, Chile
[7] Joint ALMA Observatory, JAO Alonso de Córdova 31070, Vitacura, Santiago de Chile, Chile
Received 2017 October 14; revised 2017 December 7; accepted 2017 December 12; published 2018 February 1

Abstract

Spectral line surveys reveal rich molecular reservoirs in G331.512–0.103, a compact radio source in the center of an energetic molecular outflow. In this first work, we analyze the physical conditions of the source by means of CH₃OH and CH₃CN. The observations were performed with the APEX Telescope. Six different system configurations were defined to cover most of the band within (292–356) GHz; as a consequence, we detected a forest of lines toward the central core. A total of 70 lines of A/E–CH₃OH and A/E–CH₃CN were analyzed, including torsionally excited transitions of CH₃OH ($\nu_t = 1$). In a search for all the isotopologues, we identified transitions of ^{13}CH₃OH. The physical conditions were derived considering collisional and radiative processes. We found common temperatures for each A and E symmetry of CH₃OH and CH₃CN; the derived column densities indicate an A/E equilibrated ratio for both tracers. The results reveal that CH₃CN and CH₃OH trace a hot and cold component with $T_k \sim 141$ K and $T_k \sim 74$ K, respectively. In agreement with previous ALMA observations, the models show that the emission region is compact ($\lesssim 5''5$) with gas density $n(H_2) = (0.7-1) \times 10^7$ cm^{-3}. The CH₃OH/CH₃CN abundance ratio and the evidences for prebiotic and complex organic molecules suggest a rich and active chemistry toward G331.512–0.103.

Key words: ISM: molecules – molecular processes – radio lines: ISM

1. Introduction

G331.512–0.103 is one of the most luminous and energetic molecular outflows known in the Galaxy. All of the system is embedded in a star-forming region known as G331.5-0.1, located in the Norma spiral arm at a distance of ∼7 pc. This source exhibits typical H II region properties and intense maser emission of OH and CH₃OH (Caswell 1998; Nyman et al. 2001; Bronfman et al. 2008). At the center of the system, a young and massive stellar object drives a bipolar flow of around 55 $M_\odot$ with a momentum of ∼2.4 × 10³ $M_\odot$ km s⁻¹. Radio continuum observations have revealed a compact and central structure associated with a dust core. The central region has been also mapped with ALMA observations with transitions of SiO (8–7), H¹³CO⁺ (4–3), HCO⁺ (4–3) and CO (3–2). The observations revealed a ring-like structure, consistent with a cavity, and the existence of a high-velocity outflow emission confined in a region lower than 5″ in size (Merello et al. 2013a, 2013b; Hervías et al. 2015). In this work, we present new results on the emission of CH₃OH and CH₃CN detected toward the central core, denominated hereafter as G331.

As an interstellar laboratory, G331 exhibits active chemistry in prebiotic and complex organic molecules likely stimulated by physical processes in the molecular core and outflow. With the Atacama Pathfinder EXperiment APEX Telescope, we detected a vast number of molecular lines potentially linked to reservoirs traced by CH₃OH and CH₃CN. Those tracers are excellent candidates to unveil the different physical components that O- and N-bearing molecules can reveal toward hot

molecular cores (Sandell et al. 1994; Wyrowski et al. 1999; Jørgensen et al. 2004; Beuther et al. 2005; Fontani et al. 2007; Fuente et al. 2014; Giannetti et al. 2017). In addition, from a chemical point of view, CH₃OH and CH₃CN are considered as parent and daughter molecules, respectively, in the route of interstellar molecular formation (e.g., Nomura & Millar 2004). With that motivation, we started a systematic study of G331 beginning with spectral analyses of A/E–CH₃OH and A/E–CH₃CN.

1.1. The Tracers CH₃CN and CH₃OH

CH₃CN (methyl cyanide) is a symmetric top molecule. The nuclear spin state of the hydrogen atoms defines whether the molecule has an ortho (E) or para (A) symmetry. Rotational levels of CH₃CN are characterized by two quantum numbers: the total angular momentum (J) and its projection on the axis of symmetry (K). Spectral signatures are associated to K-ladder structures whose notation for the A and E configurations are $K = 3n$ and $K = 3n \pm 1$, respectively (Solomon et al. 1971; Boucher et al. 1980; Cummins et al. 1983).

CH₃OH (methanol) is one of the simplest asymmetric-top molecules; however, its spectrum is quite complicated because there is a strong coupling between torsional and vibrational modes. Methanol also exists in two species denoted as A and E depending on the nuclear spin alignment of the three H-atoms of the methyl group (CH₃). The energy levels of methanol can be assigned with the total angular momentum J and its component K along the symmetry axis (Lees & Baker 1968; Lovas et al. 1982).

Table 1
List of Setups Observed with the APEX-2 SHeFI Instrument Toward G331

Setup Centered at	Frequency (GHz)	Beam ($''$)	Resolution (10^{-2} km s^{-1})
CH$_3$CN (16–15)	292–296	21.4	7.7
CH$_3$CN (19–18)	329–333	19.0	6.9
CH$_3$OH (7–6)	336–340	18.6	6.8
SO (8–7)	343–347	18.2	6.6
CH$_3$OCH$_3$ (11–10)	347–351	17.9	6.5
HCOOCH$_3$ (33–32)	352–356	17.7	6.4

The excellent spectral resolution of the used instrument allowed us to separately study the A and E isomers of CH$_3$CN and CH$_3$OH. Nuclear spin conversion of A and E symmetries are considered to be rare events, being affected by chemical reactions, non-reactive collisions and grain-surface mechanisms (Willacy et al. 1993; Hugo et al. 2009). However, the spin conversion has a particular relevance in molecular astrophysics. Important questions remain unsolved: for instance, how collisions stimulate conversions and, as a consequence, if that property can be used as an astronomical clock (Lee et al. 2006; Sun et al. 2015). One of our goals is to verify if the A and E pairs are equally populated at the local temperature of the source (e.g., Andersson et al. 1984; Minh et al. 1993; Wirström et al. 2011).

We organized this paper as follows. In Section 2, the observational procedure is described. In Section 3, results about the line identification are presented. In Section 4, we discuss the radiative analysis. The discussion, conclusions, and perspectives are presented in Sections 5 and 6.

2. Observations and Methodology

The observations were carried out in 2016 March with the Atacama Pathfinder Experiment Telescope (APEX), located at *Llano de Chajnantor* (Chilean Andes). The spectra were obtained using the single point mode toward the coordinates R.A., decl. (J2000) = $16^h12^m10^s.1$, $-51°28'38''.1$. We used the APEX-2 receiver of the Swedish Heterodyne Facility Instrument (SHeFI) as front end (Güsten et al. 2006; Risacher et al. 2006). The employed back end was the eXtended bandwidth Fast Fourier Transform Spectrometer2 (XFFTS2), which consists of two units with a bandwidth of 2.5 GHz divided in to 32768 channels. We selected six setups to cover a band ranging from 292 GHz to 356 GHz; they are summarized in Table 1. The integration time was estimated to obtain a conservative rms noise of $\sim$25 mK; then each setup expended integration times between 0.7 and 2.6 hs, with system temperatures in the range of $T_{sys} \sim$ (200–380) K.

The calibration was done applying the chopper-wheel technique. The output intensity provided by the system was obtained in a scale of T_A^*, which represents the antenna temperature corrected by atmospheric attenuation. The observed intensities were converted to the main-beam temperature scale using $\eta_{mb} = 0.73$, the main-beam efficiency for APEX-2 (Güsten et al. 2006).

All the K-ladders structures appeared closely spaced in a wide range of frequencies so that they were observed with the same receiver. This helped us inspect irregularities due to calibration uncertainties, for which we adopted an error of 20%.

The data reduction was carried out with the CLASS package of the GILDAS software.[8] The line identification was performed using the NIST[9] (Lovas et al. 2009), CDMS[10] (Müller et al. 2005), and JPL[11] (Pickett et al. 1998) spectroscopy databases. Specifically, the CDMS and JPL catalogs were interactively loaded on the survey using the Weeds extension of CLASS. The radiative analyses were performed using the CASSIS software.[12]

3. Results

3.1. A/E–CH$_3$CN

We observed the transitions CH$_3$CN $J = 16$–15, $J = 18$–17, and $J = 19$–18; a set of them is displayed in Figure 1. Within those levels, the spectral resolution was high enough to separate the components $K = 0$, 3, 6, and 9 from $K = 1$, 2, 4, 5, 7 and 8, which correspond to A–CH$_3$CN and E–CH$_3$CN, respectively (see Table 2).

The line identification was performed overlapping the laboratory values on the observed spectral bands at the rest velocity of the source. A high coincidence was obtained, as the K-ladder structures appeared separately and well centered, at the source's rest frequency (with $V_{lsr} = -90$ km s^{-1}), as predicted by the spectroscopic databases (Figure 1). This inspection revealed that most of the lines have a Gaussian profile, but only a few of them presented broad blue and red wings due to the outflow activity. We applied Gaussian functions to fit and model the emission. For that, the spectral line processing was carried out using the CLASS package, by means of which we fitted baselines and Gaussian functions for each processed line. As a result, in Table 2 we listed the Gaussian fit parameters and uncertainties of each analyzed line; those parameters are the integrated line flux ($\int T_{mb} dV$ in K km s^{-1}), local standard of rest (LSR) velocity (V_{lsr} in km s^{-1}), and the line width given by the FWHM (FWHM in km s^{-1}).

From a simple comparison of the A–CH$_3$CN fluxes, we observed a stiff increase of them as the lines go from the $K = 6$ to $K = 0$ transitions. This behavior is in agreement with the probabilities predicted by the Einstein coefficients (A_{ij}). For the transitions with $J_{up} = 16$, 18, and 19, the obtained patterns are 16_6:16_3:$16_0 \approx$ 1:3:4, 18_6:18_3:$18_0 \approx$ 1:4:6, and 19_6:19_3:$19_0 \approx$ 1:1:2, respectively. Only few transitions diverged from this pattern, namely, A–CH$_3$CN $J = 18_6 - 17_6$, and $J = 19_3 - 18_3$, whose emission appeared blended with HNCO ($15_{1,14} - 14_{1,13}$) and C$_2$H ($4_{4,4} - 3_{3,2}$) at 330848 MHz and 349400 MHz, respectively. Those contaminant transitions were previously detected by Jewell et al. (1989) and Sutton et al. (1991) in Orion A and OMC-1.

For E–CH$_3$CN lines, the derived fluxes also increase when the K-ladders vary from seven to one. This is in agreement with the spontaneous decay rates predicted by A_{ij}. For the transitions with $J_{up} = 16$, 18, and 19, the complete patterns are 16_7:16_5:16_4:16_2:$16_1 \approx$ 1:2:3:5:10, 18_7:18_5:18_4:18_2:$18_1 \approx$ 1:3:4:8:12, and 19_7:19_5:19_4:19_2:$19_1 \approx$1:7:7:12:26, respectively. Here, the transition E–CH$_3$CN $J = 19_4 - 18_4$ at 349346 MHz appeared blended with C$_2$H ($4_{5,4} - 3_{4,3}$) at 349339 MHz. We also found
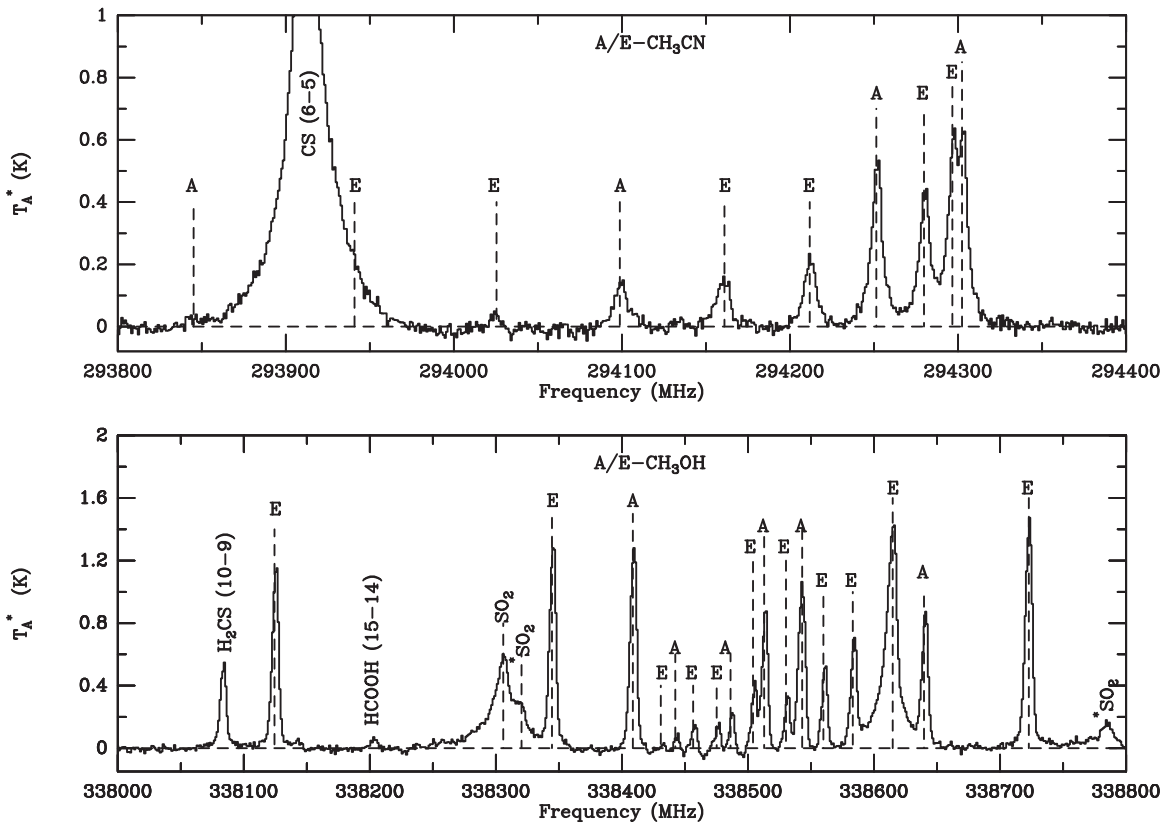

Figure 1. Lines of A/E–CH$_3$CN and A/E–CH$_3$OH as observed with the APEX-2 SHeFI instrument toward G331. Lines were adjusted to their rest frequencies using the CDMS and JPL catalogs. Due to the high intensity of the methanol lines, the range of the y-axis is different in both panels.

that the transition E–CH$_3$CN $J = 19_7 - 18_7$ at 349125 MHz might be blended with CH$_3$OCHO at 349124 MHz.

The search for the high levels $K = 8$ and $K = 9$ yielded negative results; we did not detect lines of these K-ladder numbers above the detection limit of the APEX data. For the cases A–CH$_3$CN $(16_9 - 15_9)$ and $(19_9 - 18_9)$, we did not observe emission at all. In the case of the $18_9 - 17_9$ line, we obtained a marginal flux from the Gaussian fits. This line also might be blended with c-C$_3$HD and/or *weeds*,[13] see Table 2. For the cases E–CH$_3$CN $(16_8 - 15_8)$ and $(18_8 - 17_8)$, the emission appeared fully and partially blended with CS (6–5) and ^{34}SO$_2$ $(21_2 - 21_1)$, respectively. For the $19_8 - 18_8$ transition, we did not detect emission. The results are listed in Table 2. In addition, a search for emission of CH$_3$CN ($\nu_8 = 1$) was performed with the current data set; however, we did not observe clear evidences to conclude about its presence in G331.

3.2. A/E–CH$_3$OH

As a forest of spectral lines (Figure 1), the main part of the CH$_3$OH emission has appeared only in an interval of 3 GHz along the whole survey. The lines were identified by a simple comparison of their frequencies, corrected by the source $V_{lsr} = -90$ km s^{-1}, with the rest frequencies reported in molecular databases. The methanol lines exhibit a symmetrical distribution which were fitted by simple Gaussian functions. The spectroscopic and fit parameters estimated for these lines are listed in Table 3. We find a FWHM of around 5.5 km s^{-1} and a $V_{lsr} = -90$ km s^{-1} with a dispersion of ± 2km s^{-1},

mainly due to lines which exhibited a low signal-to-noise ratio (S/N). In Figure 1, we show a set of A and E–CH$_3$OH lines with $J = 7$–6.

Although most of the methanol emission corresponds to the torsional ground state, we also identified lines corresponding to the first excited state ($\nu_t = 1$). Such is the case for the lines displayed in Figure 2 (upper panel), where it is observed a broad line of ^{34}SO at $\sim$337580 MHz blended with the transition E–CH$_3$OH ($\nu_t = 1$) $7_4 - 6_4$ at a frequency, corrected by the source V_{lsr}, of 337581.663 MHz. Around the ^{34}SO peak, minor satellite emission also was identified as corresponding to (A/E)-CH$_3$OH $\nu_t = 1$; the spectroscopic parameters are summarized in Table 4. In the bottom panel of Figure 2, we display the only excited line without contaminant emission, which corresponds to A–CH$_3$OH ($\nu_t = 1$) $7_1 - 6_1$ at a frequency, corrected by the source V_{lsr}, of 337969.414 MHz.

Emission of excited methanol is typically observed toward hot molecular cores. For instance, Menten et al. (1986), Sutton et al. (1995) and Schilke et al. (2001) have reported its emission in OMC-1, W3(OH), and W51.

The observed lines of excited methanol constitute an evidence for its presence in G331. However, to solve questions as whether the excited emission is populated at the same conditions of the ground state, it is necessary to carry out complementary observations; for instance, at frequencies between 600–720 GHz. These observations could reveal a larger number of CH$_3$OH $\nu_t = 1, 2$ lines favoring a better estimation on the physical conditions. In the bottom panel of Figure 2, we displayed a broad line close to 337900 MHz, which is associated to SO$_2$; however, that line could be also blended with CH$_3$OH ($\nu_t = 2$) $J = 7$–6 at 337877 MHz.

---

[13] Conventional term adopted to label species with numerous spectral lines in the mm/sub-mm regime.

Table 2
Spectral Line Analysis of A–CH_3CN and E–CH_3CN in G331

Transition	Frequency (MHz)	E_u (K)	A_{ij} $(10^{-3}\,s^{-1})$	$\int T_{mb}dV$ (K km s^{-1})	V_{lsr} (km s^{-1})	FWHM (km s^{-1})
A–CH_3CN						
[a]16_9–15_9	293845.164	697.83	1.51	…	…	…
16_6–15_6	294098.867	377.0721	1.9	2.065 ± 0.006	-90.7 ± 0.2	10.3 ± 0.5
16_3–15_3	294251.461	184.3532	2.13	5.9 ± 0.3	-90.4 ± 0.2	8.2 ± 0.6
16_0–15_0	294302.388	120.0696	2.21	7.9 ± 0.2	-89.69 ± 0.07	8.8 ± 0.2
[b]$18_9 - 17_9$	330557.569	728.67	2.36	0.15 ± 0.04	-91.2 ± 0.1	0.9 ± 0.2
[c]$18_6 - 17_6$	330842.762	407.9468	2.8	1.53 ± 0.07	-88.2 ± 0.4	10 ± 0.1
$18_3 - 17_3$	331014.296	215.2437	3.07	6.6 ± 0.5	-90.3 ± 0.3	8.9 ± 0.8
$18_0 - 17_0$	331071.544	150.9654	3.16	9.1 ± 0.3	-89.5 ± 0.1	9.4 ± 0.3
[a]$19_9 - 18_9$	348911.401	745.42	2.87	…	…	…
$19_6 - 18_6$	349212.311	424.7065	3.34	3.01 ± 0.01	-90.4 ± 0.2	11.5 ± 0.5
[d]$19_3 - 18_3$	349393.297	232.012	3.63	3.66 ± 0.07	-91.7 ± 0.3	3.8 ± 0.6
$19_0 - 18_0$	349453.7	167.7368	3.72	5.5 ± 0.3	-90.5 ± 0.1	6.8 ± 0.4
E–CH_3CN						
[e]16_8–15_8	293940.916	568.69	1.65	…	…	…
16_7–15_7	294025.496	461.7635	1.78	0.8 ± 0.1	-88.7 ± 0.6	10 ± 2
16_5–15_5	294161.001	290.5519	1.99	2.14 ± 0.09	-89.2 ± 0.2	9.8 ± 0.5
16_4–15_4	294211.873	226.3073	2.07	2.93 ± 0.08	-90.2 ± 0.1	9.3 ± 0.3
16_2–15_2	294279.75	140.6138	2.17	4.19 ± 0.09	-90.79 ± 0.08	7.9 ± 0.2
16_1–15_1	294296.728	119.1843	2.2	7.74 ± 0.07	-91.87 ± 0.07	9.4 ± 0.1
[f]$18_8 - 17_8$	330665.206	599.54	2.52	1.21 ± 0.07	-91.4 ± 0.2	8.1 ± 0.5
$18_7 - 17_7$	330760.284	492.6304	2.67	0.8 ± 0.1	-90.8 ± 0.7	11 ± 2
$18_5 - 17_5$	330912.608	321.4329	2.91	2.9 ± 0.1	-89.4 ± 0.2	11.6 ± 0.6
$18_4 - 17_4$	330969.794	257.1937	3	3.3 ± 0.1	-90.5 ± 0.1	9.2 ± 0.4
$18_2 - 17_2$	331046.096	171.5073	3.12	6.66 ± 0.09	-90.87 ± 0.07	10.4 ± 0.2
$18_1 - 17_1$	331065.181	150.0797	3.15	10.252 ± 0.007	-91.62 ± 0.06	10.6 ± 0.1
[a]$19_8 - 18_8$	349024.971	616.29	3.05	…	…	…
[g]$19_7 - 18_7$	349125.287	509.38	3.2	0.304 ± 0.003	-90.1 ± 0.6	5.9 ± 0.7
$19_5 - 18_5$	349286.006	338.1962	3.45	2.106 ± 0.008	-89.6 ± 0.2	9.5 ± 0.5
[h]$19_4 - 18_4$	349346.343	273.9599	3.55	2.091 ± 0.002	-89.76 ± 0.09	6.1 ± 0.1
$19_2 - 18_2$	349426.85	188.2773	3.67	5.3 ± 0.1	-90.61 ± 0.9	9.8 ± 0.2
$19_1 - 18_1$	349446.987	166.8506	3.71	8.018 ± 0.001	-91.76 ± 0.05	9.39 ± 0.08

Notes. Columns 1–4 list the spectroscopic parameters collected from databases such as CDMS and JPL. Columns 5–7 contain the resulting parameters and uncertainties derived from Gaussian fits; they are line flux ($\int T_{mb}dV$), local standard of rest velocity (V_{lsr}), and the line width (FWHM). [a] Marginal emission ($<5\sigma$). Likely blended lines with:
[b] $HCOOCH_2CH_3$ (330557 MHz) and/or c-C_3HD (330558 MHz).
[c] HNCO (330848 MHz).
[d] C_2H (349400 MHz).
[e] CS (293912 MHz).
[f] $^{34}SO_2$ (330667 MHz).
[g] CH_3OCHO (349124 MHz).
[h] C_2H (349339 MHz).

3.3. Isotopologues

We searched for lines of the D, ^{13}C, ^{15}N and ^{18}O isotopologues of CH_3CN and CH_3OH. As predicted by the spectroscopic databases, several frequencies of those isotopologues fall across the bands; however we only confirm the presence of $^{13}CH_3OH$. Emission related to $^{13}CH_3CN$ $J = 19–18$ was also identified; however, the lines are blended with SO $J = 3–2$ at 339341 MHz. Those lines were also reported by Jewell et al. (1989) in Orion A.

We detected a couple of transitions of A–$^{13}CH_3OH$. The associated spectroscopic parameters are presented in Table 5. The lines were identified at the rest frequencies 330252.798 MHz and 350103.118 MHz with S/N of S/N $\geqslant$ 5. Such detections have been fundamental to analyze the opacity of the detected emission. For instance, we estimated flux ratios using lines of A–$^{13}CH_3OH$ and A–CH_3OH with

comparable spectroscopy, namely using those transitions that have exhibited similar frequencies, A_{ij} and E_u values. Then, by selecting the 7_0–6_0 and 1_1–0_0 transitions both of A–CH_3OH and A–$^{13}CH_3OH$ (Tables 3 and 5), whose A_{ij} values are in agreement almost by a factor 1, we obtained the flux ratios $C/^{13}C = 18.1 \pm 0.7$ and $C/^{13}C = 17.7 \pm 0.1$, respectively. Such flux ratios are similar to the values reported in sources toward the Galactic center, where $C/^{13}C = 20$ (Wilson & Rood 1994; Requena-Torres et al. 2006). These ratios imply finite values of opacities, therefore in the subsequent sections we will take into account optical depth corrections to estimate the physical conditions derived from the CH_3OH and CH_3CN emission.

Two lines of E–$^{13}CH_3OH$ were also identified, although they exhibited contamination. Close to their rest frequencies, lines of $^{34}SO_2$ $J = 8–7$ and CH_3OCH_3 $J = 16–15$ are candidates for blended emission. These contaminants were also detected

Table 3
The Table 2 Caption Applies Here for A–CH$_3$OH and E–CH$_3$OH

Transition J_k	Frequency (MHz)	E_u (K)	A_{ij} (10^{-5} s^{-1})	$\int T_{mb}dV$ (K km s^{-1})	V_{lsr} (km s^{-1})	FWHM (km s^{-1})
A–CH$_3$OH						
6_1–5_1	292672.889	63.707	10.6	6.95 ± 0.06	-90.67 ± 0.02	5.24 ± 0.05
3_2–4_1	293464.055	51.6381	2.89	3.39 ± 0.09	-90.35 ± 0.09	6.8 ± 0.2
12_2–11_3	329632.881	218.8033	6	0.59 ± 0.07	-89.8 ± 0.3	4.1 ± 0.6
11_1–11_0	331502.319	169.0101	19.6	3.394 ± 0.001	-90.17 ± 0.02	2.82 ± 0.03
[a]7_3–8_1	332920.822	114.794	1.15×10^{-5}	...	...	...
12_1–12_0	336865.149	197.0765	20.3	6.9 ± 0.5	-91.9 ± 0.2	6.9 ± 0.3
7_0–6_0	338408.698	64.9817	17	10.83 ± 0.07	-90.51 ± 0.02	5.31 ± 0.04
7_6–6_6	338442.367	258.6994	4.53	1.09 ± 0.06	-91.3 ± 0.1	5.7 ± 0.4
7_5–6_5	338486.322	202.8864	8.38	2.11 ± 0.08	-90.98 ± 0.09	4.9 ± 0.2
7_2–6_2	338512.853	102.7032	15.7	7.3 ± 0.4	-90.5 ± 0.1	5.5 ± 0.4
7_3–6_3	338543.152	114.7948	13.9	9.21 ± 0.08	-89.77 ± 0.02	5.62 ± 0.05
7_2–6_2	338639.802	102.7179	15.7	7.4 ± 0.7	-90.6 ± 0.2	5.6 ± 0.6
2_2–3_1	340141.143	44.6729	2.79	2.14 ± 0.06	-90.71 ± 0.08	5.5 ± 0.2
[a]16_1–15_2	345903.916	332.6545	9.02	...	...	...
5_4–6_3	346204.271	115.1625	2.17	2.31 ± 0.07	-90.74 ± 0.09	5.9 ± 0.2
14_1 – 14_0	349106.997	260.2068	22	4.25 ± 0.06	-90.77 ± 0.04	5.41 ± 0.09
1_1–0_0	350905.1	16.841	33.1	12.19 ± 0.05	-90.58 ± 0.01	5.13 ± 0.03
[a]8_2–9_0	351685.48	121.2915	16.2	...	...	...
[a]10_4–11_2	355279.539	207.9929	1.22×10^{-3}	...	...	...
13_0–12_1	355602.945	211.0285	12.6	4.02 ± 0.04	-91.01 ± 0.02	4.76 ± 0.06
15_1–15_0	356007.235	295.2675	23	2.68 ± 0.05	-90.46 ± 0.05	5.8 ± 0.1
E–CH$_3$OH						
8_{-3}–9_{-2}	330793.887	138.3774	5.38	1.96 ± 0.06	-91.03 ± 0.07	4.6 ± 0.1
16_{-1}–15_{-2}	331220.371	312.7333	5.23	0.55 ± 0.06	-91.4 ± 0.3	5.3 ± 0.6
3_3–4_2	337135.853	53.7412	1.58	1.09 ± 0.06	-91.1 ± 0.1	4.7 ± 0.3
[a]7_2–6_2	337671.238	456.8285	15.5	...	...	...
[a]7_5–6_5	337685.248	486.0568	8.28	...	...	...
[a]7_{-1}–6_{-1}	337707.568	470.3161	16.5	...	...	...
7_0–6_0	338124.488	70.1794	16.9	9.09 ± 0.06	-90.74 ± 0.01	5.01 ± 0.04
7_{-1}–6_{-1}	338344.588	62.6521	16.6	9.61 ± 0.08	-90.63 ± 0.02	4.87 ± 0.05
[a]7_6–6_6	338404.61	235.8941	4.51	...	...	...
[a]7_{-6}–6_{-6}	338430.975	246.0504	4.54	...	...	...
7_{-5}–6_{-5}	338456.536	181.1017	8.34	1.3 ± 0.4	-90.9 ± 0.7	5 ± 2
7_5–6_5	338475.226	193.1625	8.34	1.5 ± 0.6	-91 ± 0.1	5 ± 3
7_{-4}–6_{-4}	338504.065	144.9961	11.5	4 ± 2	-91.3 ± 0.04	6 ± 1
7_4–6_4	338530.257	153.0934	11.5	3.1 ± 0.6	-91.1 ± 0.4	5 ± 1
7_{-3}–6_{-3}	338559.963	119.8084	14	4.5 ± 0.1	-90.93 ± 0.6	5.2 ± 0.1
7_3–6_3	338583.216	104.8115	13.9	6.9 ± 0.2	-90.99 ± 0.08	6.6 ± 0.2
7_1–6_1	338614.936	78.1537	17.1	21.4 ± 0.8	-89.5 ± 0.2	9.9 ± 0.5
7_{-2}–6_{-2}	338722.898	83.0148	15.7	12.53 ± 0.07	-90.04 ± 0.01	5.61 ± 0.03
[a]18_2–17_3	344109.039	411.5062	6.79	...	...	...

Note.
[a] Marginal emission ($<5\sigma$).

toward the Hot Molecular Core G34.3+0.15 (MacDonald et al. 1996).

4. Physical Conditions

4.1. Statistical Equilibrium Calculations

In this section, we present results based on statistical equilibrium models when considering collisions between the analyzed molecules and molecular hydrogen. To estimate the kinetic temperatures and column densities, we ran the RADEX code into CASSIS, whose formalism is analogous to the Large Velocity Gradient approximation (van der Tak et al. 2007). RADEX considers the probability that a photon escape in an isothermal and homogeneous medium without large-scale velocity fields. Collision rate data were collected from the LAMDA database.[14]

Conjointly with RADEX/CASSIS, we used the Markov Chain Monte Carlo (MCMC) method to simulate the observed lines from the resulting best solutions, which are given by the minimal χ^2 value. The MCMC algorithm operates on values chosen randomly within a sample defined by a minimum and maximum limit for an N-dimensional parameter space. This characteristic is the most relevant when calculations require as inputs several free parameters. In detriment, the quality of the fit is a monotonically increasing function of the number of iterations introduced in the chain, which in turn affects the

---

[14] Leiden Atomic and Molecular Database LAMDA, http://home.strw.leidenuniv.nl/moldata/.

Table 4
The Table 2 Caption Applies Here for A–CH$_3$OH ($\nu_t = 1$) and E–CH$_3$OH ($\nu_t = 1$)

Transition J_k	Frequency (MHz)	E_u (K)	A_{ij} (10^{-5} s^{-1})	$\int T_{mb} dV$ (K km s^{-1})	V_{lsr} (km s^{-1})	FWHM (km s^{-1})
A–CH$_3$OH ($\nu_t = 1$)						
[a]7_5–6_5	337546.048	485.4	8.13	1.047 ± 0.004	-92.8 ± 0.3	9.1 ± 0.5
[a]7_2–6_2	337625.679	363.5	15.5	10.2 ± 0.9	-90.5 ± 0.3	8 ± 1
[a]7_2–6_2	337635.655	363.5	15.5	1.2 ± 0.2	-92.6 ± 0.6	9 ± 2
7_1–6_1	337969.414	390.1	16.6	0.39 ± 0.05	-90.8 ± 0.3	5.2 ± 0.7
E–CH$_3$OH ($\nu_t = 1$)						
[a]7_4–6_4	337581.663	428.2	11.3	…	…	…
[a]7_{-2}–6_{-2}	337605.255	429.4	15.6	1.513 ± 0.003	-89.8 ± 0.3	11.7 ± 0.5
[a]7_0–6_0	337643.864	365.4	16.9	1.1 ± 0.8	-90.2 ± 0.2	5.9 ± 0.5
[b]10_{-2}–11_{-3}	344312.267	491.91	17.7	…	…	…

Note. Transitions and quantum numbers from Xu & Lovas (1997) and references therein. Likely blended lines with:
[a] ^{34}SO 8_8–7_7 (337580 MHz).
[b] SO 8_8–7_7 (344310 MHz).

Table 5
Spectroscopic and Observational Parameters of the of the $A-^{13}$CH$_3$OH Lines Analyzed in G331

Transition J_k	Frequency (MHz)	E_u (K)	A_{ij} (10^{-5} s^{-1})	$\int T_{mb} dV$ (K km s^{-1})	V_{lsr} (km s^{-1})	FWHM (km s^{-1})	[a]C/^{13}C
7_0–6_0	330252.798	63.4	15.8	0.60 ± 0.07	-90.7 ± 0.3	5.0 ± 0.6	18.1 ± 0.7
1_1–0_0	350103.118	16.8	32.9	0.69 ± 0.05	-91.2 ± 0.2	4.3 ± 0.3	17.7 ± 0.1

Note. Similarly, the Table 2 caption applies here.
[a] Flux ratios derived by considering the integrated fluxes of A–CH$_3$OH (7_0–6_0) and (1_0–0_0) listed in Table 3.
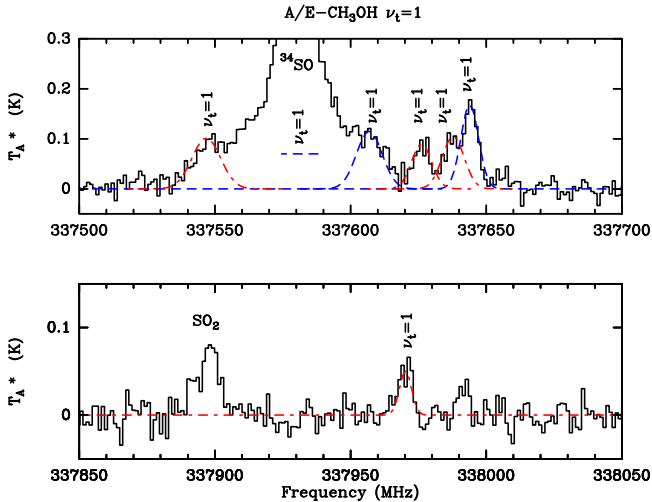
Figure 2. Panels showing the torsional excited lines of A–CH$_3$OH (red dashed–dotted line) and E–CH$_3$OH (blue dashed line) against the spectra of G331 (black histogram). In increasing order, the Gaussian fits are centered at the rest frequencies ∼337546 MHz, 337581 MHz (blended with ^{34}SO), 337605 MHz, 337625 MHz, 337635 MHz, 337643 MHz, and 337969 MHz.

"computational time" to achieve convergence (e.g., Guan & Krone 2007; Foreman-Mackey et al. 2013; Tahani et al. 2016).

We prepared MCMC routines for each A and E species. The numerical sample explored by the algorithm was delimited by five free parameters: kinetic temperature (T_k), column density (N), source size (θ), FWHM and hydrogen density (n_{H_2}). To guarantee that the code has visited the sample, we tested routines with number of iterations of the order of 10^5. Once the

algorithm achieves convergence, the minimal χ^2 is computed printing the statistical results for each parameter. This methodology implied large run-times. As a total, we modeled seven and 13 lines of A–CH$_3$CN and E–CH$_3$CN, respectively, and 10 and 13 lines of A–CH$_3$OH and E–CH$_3$OH, respectively. The statistical calculations are summarized in Table 6. Likewise, the best-fit model lines are exhibited in Figure 3.

There are two aspects that were common for the models of A/E–CH$_3$OH and A/E–CH$_3$CN. First, we obtained H$_2$ densities in the interval $n_{H_2} = (0.7$–$1) \times 10^7$ cm^{-3}, which is in agreement within a factor $\gtrsim 1.5$ with the density derived from the dust continuum (Hervías-Caimapo et al. submitted). Also, we intended to differentiate the densities of the ortho-H$_2$ and para-H$_2$ collisional partners (o-H$_2$ and p-H$_2$, respectively). Although studies explain the differences when A and E species collide with o-H$_2$ and p-H$_2$ (e.g., Rabli & Flower 2010), for our purposes we just conclude that the o-H$_2$/p-H$_2$ ratio varied between ∼0.6 and 1.0 for the different MCMC computations. That interval is consistent with the ortho-to-para limit of 0.2, when H$_2$ is thermalized at the CO temperature, and ortho-to-para limit of three when H$_2$ first forms (Flower & Watt 1984; Lacy et al. 1994).

The second aspect is that the modeled spectral lines yielded source sizes in agreement with a compact emitter region. For CH$_3$CN and CH$_3$OH we found sizes of ∼4″5 and ∼5″3, respectively. This result is supported by previous CO (7–6) maps obtained with the Australia Telescope Compact Array (ATCA), for which Bronfman et al. (2008) determined a compact and dense region of ∼4″3. Merello et al. (2013a, 2013b) mapping the emission traced by SiO (8–7) found a ring-type structure of $\lesssim 5''$.
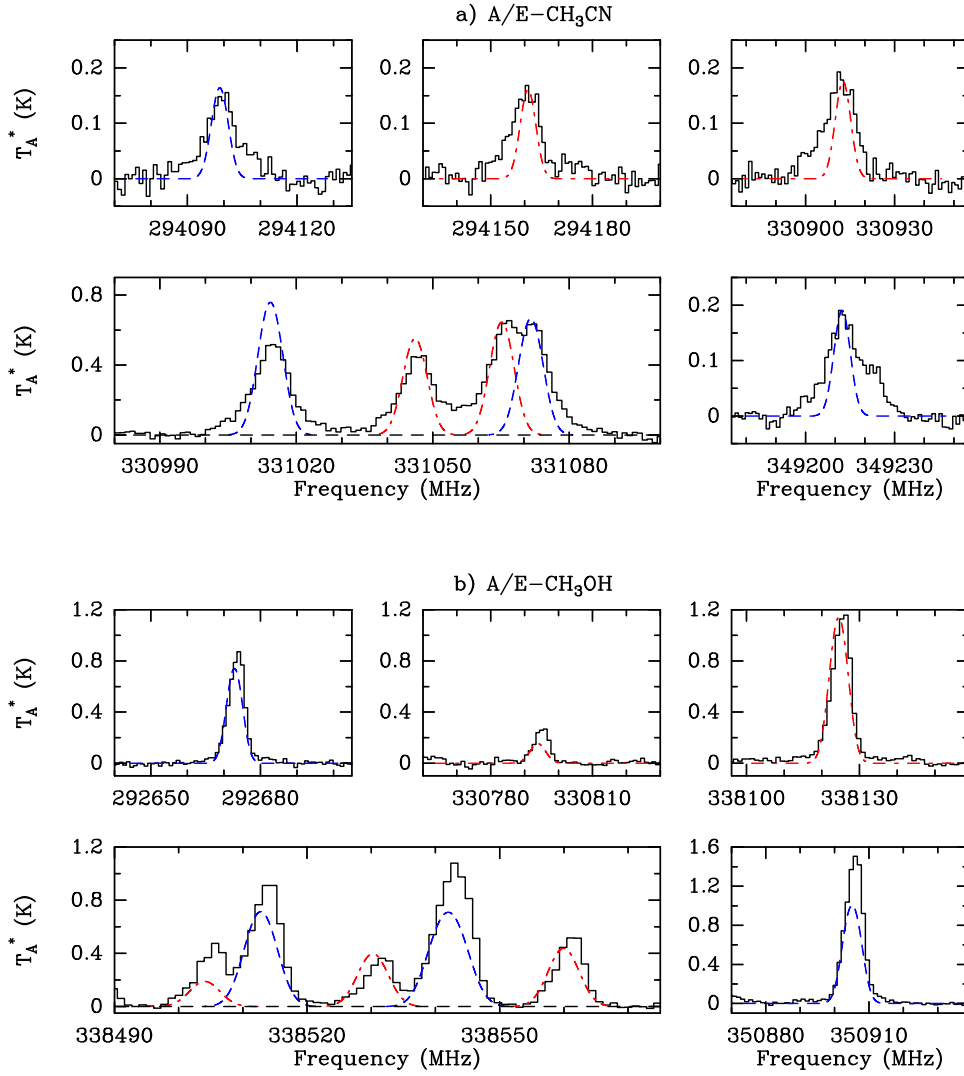
Figure 3. Spectral lines and the best fits assuming non-LTE conditions, plotted as a function of the frequency corrected by the source V_{lsr}, of (a) A–CH_3CN (blue dashed line) and E–CH_3CN (red dashed–dotted-line) and (b) A–CH_3OH (blue dashed line) and E–CH_3OH (red dashed–dotted-line). For A/E–CH_3CN, the models yielded a kinetic temperature between $\sim(140$–$142)$ K and column densities between $\sim(3.7$–$4.8) \times 10^{14}$ cm^{-2}. For A/E–CH_3OH, the models yielded a kinetic temperature between $\sim(64$–$85)$ K and column densities between $\sim(8.5$–$9.8) \times 10^{15}$ cm^{-2}.

Table 6
Parameters and Physical Conditions Derived
from the Statistical Equilibrium Calculations that have Yielded Hydrogen
Densities between 0.7 and 1×10^7 cm^{-3}

Parameters	A–CH_3CN	E–CH_3CN	A–CH_3OH	E–CH_3OH
Modeled lines	7	13	10	13
χ^2 min	5.69	7.77	6.23	4.42
FWHM (km s^{-1})	5.49 ± 0.01	5.49 ± 0.01	4.9 ± 0.1	4.88 ± 0.01
N (10^{14} cm^{-2})	4.77 ± 0.05	3.69 ± 0.04	85 ± 20	98 ± 0.1
T_k (K)	142.1 ± 0.9	140.5 ± 0.3	64 ± 2	84.8 ± 0.1
θ ($''$)	4.51 ± 0.01	4.53 ± 0.02	5.7 ± 0.3	5.01 ± 0.04

Note. The number of computed lines and the reduced χ^2 values have also been included.

4.2. LTE Analysis

Rotational diagrams were constructed to estimate the excitation temperatures (T_{exc}) and column densities (N) of A/E–CH_3CN and A/E–CH_3OH. Assuming that the emission is optically thin and uniformly fills the antenna beam, T_{exc} and N can be calculated from

$$\ln\left(\frac{N_u}{g_u}\right) = \ln\left(\frac{N}{Z}\right) - \frac{E_u}{kT_{exc}}, \qquad (1)$$

where N_u/g_u and E_u are the column density per statistical weight and the energy of the upper level, respectively, and Z is the partition function (Goldsmith & Langer 1999). In local thermodynamic equilibrium (LTE), Equation (1) represents a Boltzmann distribution whose values $\ln N_u/g_u$ versus E_u/k can be fitted using a straight line, whose slope is defined by the term $1/T_{exc}$.

The rotational diagrams were constructed taking a beam dilution factor associated with a point-like emitter region. Therefore, a correction that is provided by the term $\ln(\Delta\Omega_a/\Delta\Omega_s)$ was introduced on the right-hand side of Equation (1) (Goldsmith & Langer 1999). This ratio relates the subtended angle of the source with the solid angle of the antenna beam. The beam dilution factor that we introduced is
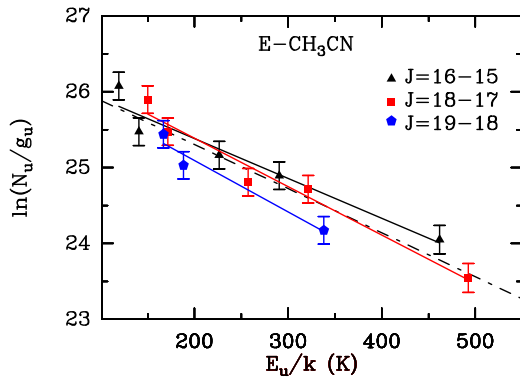
Figure 4. Rotational diagram fits of E–CH_3CN across all the K-ladder levels (dashed-dotted line), yielding $N \simeq 7.5 \times 10^{14}$ cm^{-2} and $T_{exc} \simeq 172$ K, and within each K-ladder structure for the transitions $J = 16$–15 (black triangles), $J = 18$–17 (red squares), and $J = 19$–18 (blue pentagons).

based on the results derived from the RADEX/MCMC calculations. Then, for CH_3CN and CH_3OH, we adopted averaged source sizes of $4\rlap{.}''5$ and $5\rlap{.}''3$, respectively.

Because the lines observed in this work fell in a broad band, from 290 to 350 GHz, yielding different beamwidths, the adopted sizes have been used in the comparisons between temperatures and column densities for the different lines.

Depending on the density of the region, the K-ladder structures of CH_3CN and CH_3OH can exhibit an important scattering of ($\ln N_u/g_u$, E_u) values in their rotational diagrams. More generally, it is expected that the higher is the gas density, the lower is the K-ladder segregation (Olmi et al. 1993; Cesaroni et al. 1997; Goldsmith & Langer 1999; Remijan et al. 2004; Araya et al. 2005; Cuadrado et al. 2017). To check the amount of scatter, we compared the rotational diagrams when they were individually constructed for each J_K level and with those obtained when an unique fit was determined across all the K-levels. As a result, we did not observe considerable discrepancies between the two cases; temperatures and column densities were found within the adopted uncertainty from calibration (Section 2). For instance, in Figure 4 we display the result for E–CH_3CN.

Optical Depth Correction

The rotational diagrams obtained from the A/E–CH_3CN and A/E–CH_3OH lines are displayed in Figure 5. They were constructed selecting only the transitions in the ground state and without contaminant emission. So far, the rotational diagrams have been scaled only considering the beam dilution factor. However, they represent a solution under the assumption of emission optically thin, $\tau \ll 1$. To revise how different the LTE solutions are from a radiative scenario with finite values of optical depths, we have applied an optical depth correction on the rotational diagrams of A/E–CH_3CN and A/E–CH_3OH. Expressed mathematically, the correction consisted in including the term $-\ln C_\tau$, with $C_\tau = \tau/1 - \exp^{-\tau}$, on the right-hand side of Equation (1) (Goldsmith & Langer 1999; Gibb et al. 2000; Remijan et al. 2004; Araya et al. 2005). Thus, the ordinates of our rotational diagrams were readjusted considering a term associated with the photon escape probability.

We have performed this adjust based on (first) the results obtained from the statistical equilibrium calculations. In the case of CH_3CN, transitions with $K = 0$, 1, 2 and 3 were the

most affected with $\tau \approx 1$. And, (second) considering the flux ratio $C/^{13}C \lesssim 20$ as we described in Section 3.3, which suggests finite optical depths.

To perform the optical depth correction, we used CASSIS which executes iterative calculations of C_τ adjusting the level populations until achieving a consistent solution. With these corrections, slight changes are expected in the LTE solutions. For instance, Araya et al. (2005) obtained differences around 10 and 14% in the temperature and column density of CH_3CN when the optical depth correction was applied, respectively.

The A/E–CH_3CN rotational diagrams (RDs), with the optical depth correction, are displayed in the upper panels of Figure 5. For A–CH_3CN, we obtained $N = (6.4 \pm 2.0) \times 10^{14}$ cm^{-2} and $T_{exc} = 156 \pm 25$ K. For E–CH_3CN, we obtained $N = (8.4 \pm 2.0) \times 10^{14}$ cm^{-2} and $T_{exc} = 152 \pm 20$ K. The percentage difference of N and T_{exc}, with respect to the RD without the optical depth correction, are ranged between (5–14)% and (2–12)%, respectively.

The A/E–CH_3OH RDs, with the optical depth correction, are displayed in the lower panels of Figure 5. For A–CH_3OH, we obtained $N = (1.9 \pm 0.5) \times 10^{16}$ cm^{-2} and $T_{exc} = 71 \pm 10$ K. For E–CH_3OH, we obtained $N = (2.0 \pm 0.1) \times 10^{16}$ cm^{-2} and $T_{exc} = 68 \pm 8$ K. The percentage difference of N and T_{exc}, with respect to the RD without the optical depth correction, are ranged between (10–22)% and (9–17)%, respectively.

We detected two lines of $^{13}CH_3OH$ (Table 5). In the absence of collisional coefficients, those lines were modeled assuming LTE conditions applying the MCMC method leaving various inputs as free parameters: N, T_{exc}, FWHM, and θ. However, we put an upper limit of $N < 5 \times 10^{15}$ cm^{-2}, which was derived from the column density of the main isotopologue and considering the ratio $C/^{13}C \lesssim 20$. The results were consistent with the physical conditions of the main isotopologue. The best LTE models are displayed in Figure 6, whose solution ($\chi^2 = 2.82$) yielded $N = (1.01 \pm 0.06) \times 10^{15}$ cm^{-2} and $T_{exc} = 89.5 \pm 0.4$ K for a modeled source size of $5\rlap{.}''7$. Additionally, the resulting FWHM values (~ 4.4 km s^{-1}) are consistent with the resulting fits reported in Table 5.

5. Discussion

5.1. Molecular Abundances

CH_3OH is more abundant and traces a region about 70 K colder than that traced by CH_3CN. From the LTE and non-LTE analysis, we found that the ratio $(A + E)$-$CH_3OH/(A + E)$-CH_3CN is about 25, indicating almost the same overabundance of A and E–CH_3OH over A–CH_3CN and E–CH_3CN.

ALMA observations of the ion $H^{13}CO^+$ (4–3) probed the existence of a core and various clumpy structures in G331 (Hervías-Caimapo et al. submitted). Maps of SiO (8–7) show as well an internal cavity surrounded by molecular emission confined in $\lesssim 5''$, for which these authors have estimated $N(H^{13}CO^+) \approx (1.5$–$3) \times 10^{13}$ cm^{-2} (e.g., Bronfman et al. 2008; Merello et al. 2013a, 2013b). The column densities of CH_3OH and CH_3CN were divided by $N(H_2)$ values to obtain their abundances. Following the works cited above, to estimate a scaled density of H_2 in G331, we applied the ratio $H^{13}CO^+/H_2 = 3.3 \times 10^{-11}$ of Orion KL (e.g., Blake et al. 1987) on the $H^{13}CO^+$ column densities derived for G331 (Merello et al. 2013a). As an approximation for the present work, we adopted the $H^{13}CO^+/H_2$ ratio of the Orion KL system, as this source is an excellent template for comparative
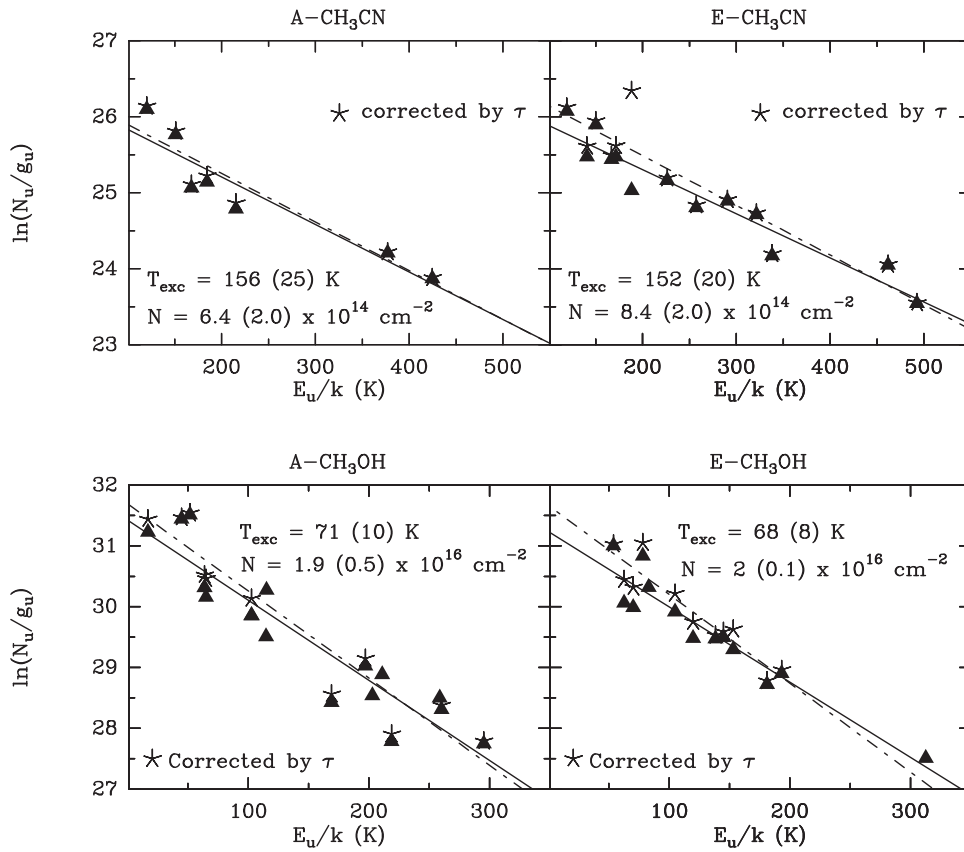
Figure 5. Upper panels: rotational diagrams of A–CH_3CN and E–CH_3CN showing the least-square fits with the optical depth correction, represented with the asterisk symbols and dashed-dotted lines, and without the optical depth correction, represented with the filled triangles and solid lines. Bottom panels: the same as above for A–CH_3OH and E–CH_3OH. Column densities and excitation temperatures correspond to the results when applied the optical depth correction, numbers in parenthesis represent uncertainties on the last digit.

Table 7
Abundances of CH_3OH and CH_3CN Derived from the LTE and Non-LTE Analysis

Method	Hot Component			Cold Component		
	$[CH_3CN]$ 10^{-9}	$[^{13}CH_3CN]$ 10^{-9}	$\%_{A-CH_3CN}$ $\approx$	$[CH_3OH]$ 10^{-9}	$[^{13}CH_3OH]$ 10^{-9}	$\%_{A-CH_3OH}$ $\approx$
non-LTE	1.8 ± 0.2	⋯	56	38 ± 10	⋯	46
LTE	3.1 ± 0.6	$\lesssim 0.08$	43	81 ± 15	$\lesssim 2.1$	49

Note. We have included the contribution of each spin isomer as a percentage of the total abundance, assumed as the sum $A+E$ of the symmetries.
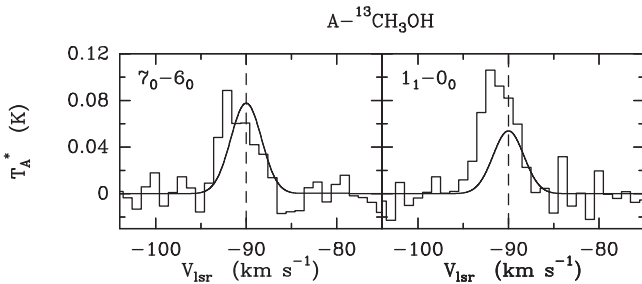
Figure 6. Spectral lines and LTE models of A–$^{13}CH_3OH$ represented by black histograms and Gaussian curves, respectively. Lines 7_0–6_0 and 1_1–0_0 appeared at the rest frequencies 330252.798 MHz and 350103.118 MHz, respectively. The models were derived from a computation whose best solution provided $N = (1.01 \pm 0.06) \times 10^{15}$ cm^{-2} and $T_{exc} = 89.5 \pm 0.4$ K.

studies on abundances and molecular complexity (e.g., Schilke et al. 2001; Beuther et al. 2005). The total abundances of CH_3OH and CH_3CN are summarized in Table 7; as a total, we refer to the $A+E$ contribution from the nuclear spin symmetries (e.g., Fuente et al. 2014). Thus, the CH_3CN emission is linked to a hot core with $T_k \approx 141$ K and $\theta \approx 4.''5$, while CH_3OH traces a cold bulk medium with $T_k \approx 74$ K and $\theta \approx 5.''3$. Also in Table 7, we included the abundance uncertainties computed from the errors obtained with the radiative models (Bevington & Robinson 2003); although we listed errors of $\lesssim 25\%$, the abundance uncertainties could be of up to 40% including other sources of errors, such as the calibration uncertainty, adopted here as 20%. In Table 7, the abundances of the ^{13}C isotopologues are also listed. Although we obtained an
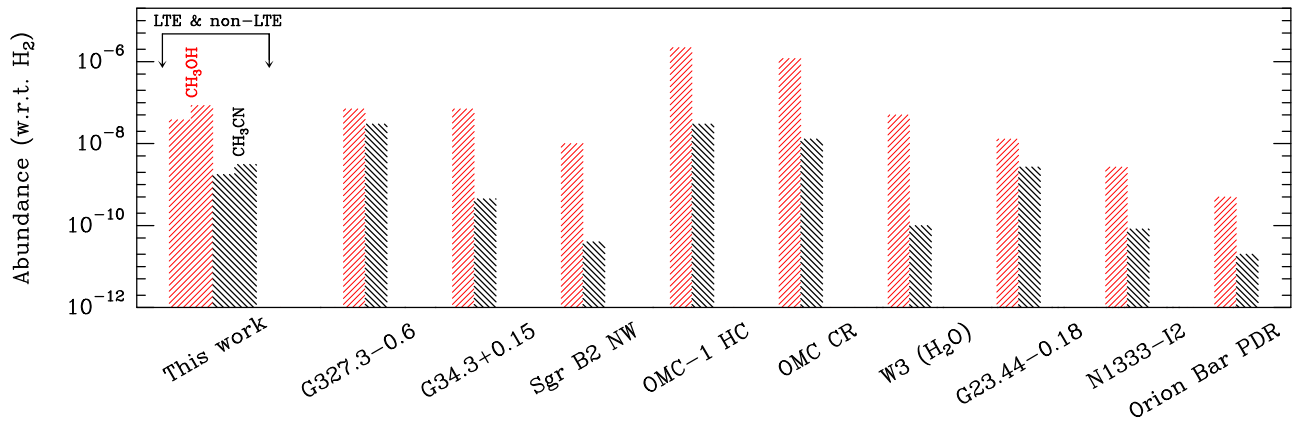
Figure 7. Comparison of the abundances of CH$_3$OH (red) and CH$_3$CN (black) in hot molecular cores, clouds, and PDR regions. Values were collected from references such as Sutton et al. (1995), MacDonald et al. (1996), Helmich & van Dishoeck (1997), Gibb et al. (2000), Nummelin et al. (2000), Jørgensen et al. (2005), Ren et al. (2011), Crockett et al. (2014), and Cuadrado et al. (2017).

inaccurate result based only on two lines of ^{13}CH$_3$OH, we found that it could be not only 20 times lower, resulting from the ^{13}C/C flux ratio, but up to 40 times under abundant than CH$_3$OH, as the LTE analysis suggested (see Figure 6). Thus, we determined [^{13}CH$_3$OH] $\lesssim 2.1 \times 10^{-9}$.

For the undetected ^{13}CH$_3$CN, we propose upper limits assuming that the ^{13}CH$_3$CN/^{13}CH$_3$OH ratio works as what we found for the main isotopologues: CH$_3$CN/CH$_3$OH $\approx 1/25$. From that conjecture, we conclude that [^{13}CH$_3$CN] $\lesssim 8 \times 10^{-11}$.

One of the goals of this work was to separately analyze the emission of the A and E spin nuclear isomers; however, the analysis indicated common physical conditions (N and T) for both spin symmetries meaning that they trace the same reservoir. The opposite case would imply spin conversion processes, induced by molecular interactions on molecular ices or collisions in gas phase, favoring an overabundance in a given spin symmetry. However, this result would be expected at earlier stages or in younger stellar sources (e.g., Minh et al. 1993; Wirström et al. 2011).

Independent of the employed analysis, we find that both the A and E isomers contribute with approximately half of the total emission of CH$_3$OH and CH$_3$CN. The percentage derived from both methods are listed in Table 7, as explained above, assuming a total abundance as $A+E$. As a similar result, MacDonald et al. (1996) determined the ratio [A–CH$_3$OH]/ [E–CH$_3$OH] ≈ 0.9 for the hot molecular core G34.3+0.15. In the envelopes around low-mass protostars, Jørgensen et al. (2005) found ortho-to-para ratios close to unity for CH$_3$OH. Recently, similar results were reported for the pairs A/E–CH$_3$CN, A/E–CH$_3$OH, and A/E–CH$_3$CHO in the Orion Bar photodissociation region (PDR; Cuadrado et al. 2017).

This tendency is similar to another aspect aimed to examine in this study: whether o- and p-H$_2$ collisional partners may affect the population of the A and E nuclear spin isomers of CH$_3$OH and CH$_3$CN. However, the MCMC/RADEX computations yielded H$_2$ ortho-to-para ratios close to unity.

Laboratory studies have offered new measurements about spin conversion, generally assumed as improbable processes. In gas phase, Sun et al. (2015) found that molecular collisions induce the interconversion of spin in molecules of methanol exhibiting a rate that decreases as the pressure increases with the number of collisions. A quantum relaxation mechanism explains the interconversion. In condensed phase, Lee et al.

(2006) observed that methanol can suffer a slow conversion from the E to the A symmetry when it is trapped in a solid matrix of p-H$_2$ prepared at low temperatures (~ 5 K). In theoretical works, Rabli & Flower (2010) studied the implications of methanol colliding with o-H$_2$ and p-H$_2$, finding qualitative and quantitative differences for those cases.

As we summarized in Table 4, emission of torsionally excited methanol was also evidenced; however, only one line appeared without blended emission: A–CH$_3$OH ($\nu_t = 1$) at ~ 337969 MHz. In some studies, it has been analyzed whether excited transitions may be populated at the same LTE conditions of the ground torsional levels (e.g., Lovas et al. 1982; Menten et al. 1986; Sutton et al. 1995; Ren et al. 2011; Sánchez-Monge et al. 2014). We made a minor examination based on the unique line without contamination; however, we found that, to account for the flux, different regimes are needed with $T_{\rm exc} \gtrsim 90$ K. Complementary observations with APEX will be carried out to determine with a better precision the physical conditions of excited methanol in G331.

5.2. The Hot and Cold Components of G331

In this study, we identified two different components that could candidate G331 as a Hot Molecular Core (HMC). Other characteristics also support this hypothesis. For instance, the source is compact, harbors a massive and energetic molecular outflow, and is embedded in a H II region where masers of OH and CH$_3$OH reveal a high star formation activity. Besides, the temperatures of the gas components are above and below the limits where evaporation of icy mantles plays an important role; for instance, to explain abundances of Complex Organic Molecules and aspects related to the age of the source. The gas densities also support such classification, since we determined H$_2$ densities typical of a dense medium $(0.7$–$1) \times 10^7$ cm^{-3}.

N- and O-bearing molecules help to diagnose the presence of different gas components in HMCs (e.g., Beuther & Sridharan 2007; Fontani et al. 2007). In this first work, it is proposed that A/E–CH$_3$CN and A/E–CH$_3$OH trace a hot ($T_k \simeq 141$ K) and cold ($T_k \simeq 75$ K) component with sizes around 4″.5 and 5″.3, respectively. Such results are in agreement with ALMA observations of CO (7–6), SiO (8–7) and H^{13}CO$^+$ (4–3). The emission of these species was found to be compacted in $\sim 5''$ (Bronfman et al. 2008; Merello et al. 2013a; Hervías et al. 2015).

In Figure 7, we compare the abundances derived in this work with other sources. Our results are similar with the abundances reported in G34.3+0.15. More generally, our results suggest different abundances, physical components, and a chemical differentiation for CH_3OH and CH_3CN in G331. The high sensitivity and spectral resolution of our single-dish spectra have been useful to realize subtle differences in the line profiles of CH_3OH and CH_3CN, inspected via the V_{lsr} and FWHM parameters listed in Tables 2 and 3. In agreement with the radiative models, these spectral signatures reveal clues on the origin and size of the emitter regions. In spite of that, and as a perspective, further observations at higher spatial resolution are needed to study the spatial distribution of different tracers in G331. Also, these observations may reveal density gradients toward the core and the outflow, allowing more accurate determinations of molecular abundances.

The fact of CH_3OH being more abundant than CH_3CN is in agreement with the chemistry that has been modeled in HMCs, where these molecules are usually referred as parent and daughter species, respectively, since CH_3OH is expected to be formed at early stages in grain surfaces, via successive hydrogenation of CO, while CH_3CN appears later via reaction between HCN and CH_3^+ (Millar et al. 1997; Nomura & Millar 2004; Guzmán et al. 2013; Loison et al. 2014). Other alternatives to produce methanol are $CH_3^+ + OH \rightarrow CH_3OH$ and $CH_2 + H_2O \rightarrow CH_3OH$. They can occur when frozen mixtures of CH_4 and H_2O are bombarded with electrons (Hiraoka et al. 2006). In addition, we have found that the physical conditions traced by those molecules might explain the regimes where prebiotic and complex organic molecules have been detected, such as CH_3OCH_3, CH_3CHO, NH_2CHO, and the $C_2H_4O_2$ isomers.

Nomura & Millar (2004) performed time-dependent chemical models considering observational aspects of the hot molecular core G34.3+0.15; for instance, that CH_3CN is associated to an inner and hot core region, while CH_3OH traces the gas present in clumps (e.g., Hatchell et al. 1998; Millar & Hatchell 1998; van der Tak et al. 2000). Comparing our column densities with the temporal values calculated by those authors, an age of 10^4 years may represent the epoch for G331, when substantial quantities of daughters molecules (e.g., CH_3CN) are produced without substantially decimate their parents (e.g., CH_3OH). Preliminary results derived by us, obtained with the gas-grain chemical code Nautilus (Ruaud et al. 2016),[15] show a CH_3OH/CH_3CN ratio similar to those derived from the observations. However, these results will be presented in a subsequent work depicting the chemistry of O-bearing molecules detected in the source.

6. Conclusions and Perspectives

As an active interstellar laboratory, the G331.512–0.103 system exhibits a rich chemistry in organic and prebiotic molecules. In this first article, we analyzed around 70 lines of A/E–CH_3OH and A/E–CH_3CN toward the central region, abbreviated here as G331. Torsionally excited transitions of methanol were evidenced. Without contaminant emission, we identified the CH_3OH ($\nu_t = 1$) 7_1–6_1 transition. Likewise, two lines corresponding to $^{13}CH_3OH$ were detected at 330252.798 MHz and 350103.118 MHz.

---

[15] http://kida.obs.u-bordeaux1.fr/networks.html

The analyses were performed including collisions with H_2 and typical radiative processes under LTE conditions, namely rotational diagrams. Both analyses coincide in that CH_3OH traces a cold component, while CH_3CN traces a hotter core with kinetic temperatures of ~ 74 K and 141 K, respectively. Likewise, the best-fits indicated emitter regions of around $4\rlap{.}''5$ and $5\rlap{.}''3$ for these tracers, respectively, with gas density $n(H_2) = (0.7-1) \times 10^7$ cm^{-3}.

We treated independently each one of the nuclear spin isomers of CH_3OH and CH_3CN, and determined the ratio $(A + E)$-$CH_3OH/(A + E)$-$CH_3CN \simeq 25$. The temperatures and densities of each A and E pair suggest that they trace a same bulk and are equally populated at each local temperature. Considering that, we estimated the CH_3OH and CH_3CN abundances from the total contribution $A+E$. Under the LTE formalism, we estimated that $[CH_3OH] \approx 8.1 \times 10^{-8}$, $[CH_3CN] \approx 3.1 \times 10^{-9}$, and the upper limits $[^{13}CH_3OH] \approx 2.1 \times 10^{-9}$ and $[^{13}CH_3CN] \approx 8 \times 10^{-11}$.

Under the perspective of hot molecular cores, the CH_3OH/CH_3CN ratio could be associated with and epoch between $(10^4$–$10^5)$ years, when daughter molecules like CH_3CN start to be produced from parent molecules, such as CH_3OH.

ORCID iDs

Edgar Mendoza ⊙ https://orcid.org/0000-0001-9381-7826
Leonardo Bronfman ⊙ https://orcid.org/0000-0002-9574-8454
Jacques R. D. Lépine ⊙ https://orcid.org/0000-0002-8969-0313
Manuel Merello ⊙ https://orcid.org/0000-0003-0709-708X
Diana R. G. Gama ⊙ https://orcid.org/0000-0003-1846-3292

References

Andersson, M., Askne, J., & Hjalmarson, A. 1984, A&A, 136, 243
Araya, E., Hofner, P., Kurtz, S., Bronfman, L., & DeDeo, S. 2005, ApJS, 157, 279
Sánchez-Monge, Á., Beltrán, M. T., Cesaroni, R., et al. 2014, A&A, 569, A11
Beuther, H., & Sridharan, T. K. 2007, ApJ, 668, 348
Beuther, H., Zhang, Q., Greenhill, L. J., et al. 2005, ApJ, 632, 355
Bevington, P. R., & Robinson, K. D. (ed.) 2003, Data Reduction and Error Analysis for the Physical Sciences (3rd ed.; Boston, MA: McGraw-Hill)
Blake, G. A., Sutton, E. C., Masson, C. R., & Phillips, T. G. 1987, ApJ, 315, 621
Boucher, D., Burie, J., Bauer, A., Dubrulle, A., & Demaison, J. 1980, JPCRD, 9, 659
Bronfman, L., Garay, G., Merello, M., et al. 2008, ApJ, 672, 391
Caswell, J. L. 1998, MNRAS, 297, 215

Cesaroni, R., Felli, M., Testi, L., Walmsley, C. M., & Olmi, L. 1997, A&A, 325, 725

Crockett, N. R., Bergin, E. A., Neill, J. L., et al. 2014, ApJ, 787, 112

Cuadrado, S., Goicoechea, J. R., Cernicharo, J., et al. 2017, A&A, 603, A124

Cummins, S. E., Green, S., Thaddeus, P., & Linke, R. A. 1983, ApJ, 266, 331

Flower, D. R., & Watt, G. D. 1984, MNRAS, 209, 25

Fontani, F., Pascucci, I., Caselli, P., et al. 2007, A&A, 470, 639

Foreman-Mackey, D., Hogg, D. W., Lang, D., & Goodman, J. 2013, PASP, 125, 306

Fuente, A., Cernicharo, J., Caselli, P., et al. 2014, A&A, 568, A65

Giannetti, A., Leurini, S., Wyrowski, F., et al. 2017, A&A, 603, A33

Gibb, E., Nummelin, A., Irvine, W. M., Whittet, D. C. B., & Bergman, P. 2000, ApJ, 545, 309

Goldsmith, P. F., & Langer, W. D. 1999, ApJ, 517, 209

Guan, Y., & Krone, S. M. 2007, arXiv:math/0703021

Güsten, R., Nyman, L. Å., Schilke, P., et al. 2006, A&A, 454, L13

Guzmán, V. V., Goicoechea, J. R., Pety, J., et al. 2013, A&A, 560, A73

Hatchell, J., Thompson, M. A., Millar, T. J., & MacDonald, G. H. 1998, A&A, 338, 713

Helmich, F. P., & van Dishoeck, E. F. 1997, A&AS, 124, 205

Hervías, C., Bronfman, L., Merello, M., et al. 2015, in ASP Conf. Ser. 499, Revolution in Astronomy with ALMA: The Third Year, ed. D. Iono et al. (San Francisco, CA: ASP), 229

Hiraoka, K., Mochizuki, N., & Wada, A. 2006, in AIP Conf. Ser. 855, Astrochemistry—From Laboratory Studies to Astronomical Observations, ed. R. I. Kaiser et al. (Melville, NY: AIP), 86

Hugo, E., Asvany, O., & Schlemmer, S. 2009, JChPh, 130, 164302

Jewell, P. R., Hollis, J. M., Lovas, F. J., & Snyder, L. E. 1989, ApJS, 70, 833

Jørgensen, J. K., Hogerheijde, M. R., Blake, G. A., et al. 2004, A&A, 415, 1021

Jørgensen, J. K., Schöier, F. L., & van Dishoeck, E. F. 2005, A&A, 437, 501

Lacy, J. H., Knacke, R., Geballe, T. R., & Tokunaga, A. T. 1994, ApJL, 428, L69

Lee, Y.-P., Wu, Y.-J., Lees, R. M., Xu, L.-H., & Hougen, J. T. 2006, Sci, 311, 365

Lees, R. M., & Baker, J. G. 1968, JChPh, 48, 5299

Nyman, L.-Å., Lerner, M., Nielbock, M., et al. 2001, Msngr, 106, 40

Loison, J.-C., Wakelam, V., & Hickson, K. M. 2014, MNRAS, 443, 398

Lovas, F. J., Bass, J. E., Dragoset, R. A., & Olsen, K. J. 2009, Observed Interstellar Molecular Microwave Transitions (Gaithersburg, MD: National Institute of Standards and Technology), https://www.nist.gov/pml/observed-interstellar-molecular-microwave-transitions-version-history

Lovas, F. J., Suenram, R. D., Snyder, L. E., Hollis, J. M., & Lees, R. M. 1982, ApJ, 253, 149

MacDonald, G. H., Gibb, A. G., Habing, R. J., & Millar, T. J. 1996, A&AS, 119, 333

Menten, K. M., Walmsley, C. M., Henkel, C., et al. 1986, A&A, 169, 271

Merello, M., Bronfman, L., Garay, G., et al. 2013a, ApJL, 774, L7

Merello, M., Bronfman, L., Garay, G., et al. 2013b, ApJ, 774, 38

Millar, T. J., & Hatchell, J. 1998, FaDi, 109, 15

Millar, T. J., MacDonald, G. H., & Gibb, A. G. 1997, A&A, 325, 1163

Minh, Y. C., Irvine, W. M., Ohishi, M., et al. 1993, A&A, 267, 229

Müller, H. S. P., Schlöder, F., Stutzki, J., & Winnewisser, G. 2005, JMoSt, 742, 215

Nomura, H., & Millar, T. J. 2004, A&A, 414, 409

Nummelin, A., Bergman, P., Hjalmarson, Å., et al. 2000, ApJS, 128, 213

Olmi, L., Cesaroni, R., & Walmsley, C. M. 1993, A&A, 276, 489

Pickett, H. M., Poynter, R. L., Cohen, E. A., et al. 1998, JQSRT, 60, 883

Rabli, D., & Flower, D. R. 2010, MNRAS, 406, 95

Remijan, A., Sutton, E. C., Snyder, L. E., et al. 2004, ApJ, 606, 917

Ren, J. Z., Liu, T., Wu, Y., & Li, L. 2011, MNRAS, 415, L49

Requena-Torres, M. A., Martín-Pintado, J., Rodríguez-Franco, A., et al. 2006, A&A, 455, 971

Risacher, C., Vassilev, V., Monje, R., et al. 2006, A&A, 454, L17

Ruaud, M., Wakelam, V., & Hersant, F. 2016, MNRAS, 459, 3756

Sandell, G., Knee, L. B. G., Aspin, C., Robson, I. E., & Russell, A. P. G. 1994, A&A, 285L, L1

Schilke, P., Benford, D. J., Hunter, T. R., Lis, D. C., & Phillips, T. G. 2001, ApJS, 132, 281

Solomon, P. M., Jefferts, K. B., Penzias, A. A., & Wilson, R. W. 1971, ApJL, 168, L107

Sun, Z.-D., Ge, M., & Zheng, Y. 2015, Natur, 6877, 1

Sutton, E. C., Jaminet, P. A., Danchi, W. C., & Blake, G. A. 1991, ApJS, 77, 255

Sutton, E. C., Peng, R., Danchi, W. C., et al. 1995, ApJS, 97, 455

Tahani, K., Plume, R., Bergin, E. A., et al. 2016, ApJ, 832, 12

van der Tak, F. F. S., Black, J. H., Schöier, F. L., Jansen, D. J., & van Dishoeck, E. F. 2007, A&A, 468, 627

van der Tak, F. F. S., van Dishoeck, E. F., & Caselli, P. 2000, A&A, 361, 327

Willacy, K., Williams, D. A., & Minh, Y. C. 1993, MNRAS, 263, L40

Wilson, T. L., & Rood, R. 1994, ARA&A, 32, 191

Wirström, E. S., Geppert, W. D., Hjalmarson, Å., et al. 2011, A&A, 533, A24

Wyrowski, F., Schilke, P., Walmsley, C. M., & Menten, K. M. 1999, ApJL, 514, L43

Xu, L.-H., & Lovas, F. J. 1997, JPCRD, 26, 17